Coastal Engineering 190 (2024) 104501

Contents lists available at ScienceDirect

Coastal Engineering

journal homepage: www.elsevier.com/locate/coastaleng

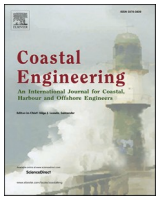

Island-based GNSS-IR network for tsunami detecting and warning

Linlin Li [a], Qiang Qiu [b,c,*], Mai Ye [b], Dongju Peng [d], Ya-Ju Hsu [e], Peitao Wang [f], Huabin Shi [g], Kristine M. Larson [h], Peizhen Zhang [a]

[a] Guangdong Provincial Key Laboratory of Geodynamics and Geohazards, School of Earth Sciences and Engineering, Sun Yat-sen University & Southern Marine Science and Engineering Guangdong Laboratory, Zhuhai, China
[b] CAS Key Laboratory of Ocean and Marginal Sea Geology, South China Sea Institute of Oceanology, Innovation Academy of South China Sea Ecology and Environmental Engineering, Chinese Academy of Sciences, Guangzhou, 510301, China
[c] China-Pakistan Joint Research Center on Earth Science, CAS-HEC, Islamabad, 45320, Pakistan
[d] Department of Land Surveying and Geo-Informatics, The Hong Kong Polytechnic University, Hong Kong, China
[e] Institute of Earth Sciences, Academia Sinica, Taipei, Taiwan
[f] Key Laboratory of Marine Hazards Forecasting, National Marine Environmental Forecasting Center, Ministry of Natural Resources, Beijing, China
[g] Faculty of Science and Technology, University of Macau, Macau
[h] Institute of Geodesy and Geoinformation, Bonn University, Bonn, Germany

ARTICLE INFO

Keywords:
Tsunami warning
GNSS-IR
Sea level measurement
Kalman filter

ABSTRACT

Deep-sea tsunami detection relies on Deep-ocean Assessment and Reporting of Tsunamis (DART), GNSS buoys, and cabled Ocean-Bottom Pressure (OBP) gauges, which are very expensive and difficult to maintain, and often suffer from vandalism or negligent damage. Here, we exploit the potential of establishing a less expensive and more robust island-based geodetic network for tsunami detecting, source reconstruction and warning. The network locates at the coastline of islands and uses a new technique: GNSS Interferometric Reflectometry (GNSS-IR). GNSS-IR retrieves sea levels from combination of the direct and reflected signals from the sea surface sent by satellites. To test the feasibility and efficiency of such a new geodetic network, we use the South China Sea region as an example, and compare its performance in reconciling the variable slip distribution on the Manila mega-thrust with the previously designed deep-sea monitoring system, i.e., DARTs and planned cable-based OBP gauges. We find that the newly designed GNSS-IR network could work equally well as the cabled OBP network in detecting tsunamis if the stations are built in strategically chosen locations. Combining GNSS-IR with a Kalman filter approach, we demonstrate that carefully situated coastal GNSS stations at global remote deep-ocean islands could function similarly to conventional tide gauges but with advantages of simultaneously measuring relative sea-level and land-height changes, meanwhile suffering lower risk from damaging sea-level events and potential vandalism.

1. Introduction

Tsunami monitoring networks, especially those located in the deep sea, are the crucial components for quickly detecting tsunami waves, validating the potential magnitudes of ensuing tsunamis. Such measurements provide timely constraints for data assimilation which is critical for reliable early warning messages (Aoi et al., 2020; Mori et al., 2022; Mulia and Satake, 2020; Tang et al., 2012; Y. Y. Wang et al., 2021; Wei et al., 2008). Since the 2004 Indian Ocean Tsunami, tsunami early warning systems have been progressively expanded from the Pacific Ocean to the Indian and Atlantic Oceans (Bernard and Titov, 2015; Mori et al., 2022). For the global tsunami observational network, the key instruments used to detect tsunami waves in the deep sea are the Deep-ocean Assessment and Reporting of Tsunamis (DART) systems: ocean-bottom pressure (OBP) sensors for tsunami detection and the moored surface buoys for real-time communication via satellites (González et al., 2005). Regionally, OBP gauges were also densely installed in cabled seafloor networks near Japan (DONET/DONET2 and *S*-NET),and near Canada (NEPTUNE) (Kanazawa, 2013; Mori et al., 2022; Mulia and Satake, 2020), but such cabled systems are excessively expensive (Bernard and Titov, 2015; González et al., 2005; Mulia and Satake, 2020). Although the DART system is very effective, vandalism is

* Corresponding author. CAS Key Laboratory of Ocean and Marginal Sea Geology, South China Sea Institute of Oceanology, Innovation Academy of South China Sea Ecology and Environmental Engineering, Chinese Academy of Sciences, Guangzhou, 510301, China.
E-mail address: qiu.qiang@scsio.ac.cn (Q. Qiu).

https://doi.org/10.1016/j.coastaleng.2024.104501
Received 13 December 2023; Received in revised form 5 March 2024; Accepted 5 March 2024
Available online 12 March 2024

a big challenge (Data Buoy Cooperation Panel, 2011). Because vandalism of tsunami buoys is very common globally, which significantly increases the already high maintenance cost. According to the report provided by Intergovernmental Oceanographic Commission of UNESCO, nearly half of DART ocean observing systems were damaged during 2006–2010 (Data Buoy Cooperation Panel, 2011). Using the tsunami warning system of the South China Sea (SCS) as an example, China has established the SCS Tsunami Advisory Center that has been fully in operation since Nov 5, 2019 (Xu et al., 2021). Great efforts have been made to install DART buoys at strategically designed locations (red-filled squares D1 and D2 in Fig. 1), but they were eventually vandalized or damaged, resulting in a complete absence of deep-sea observing instruments in the SCS. A similar situation occurred in the Indian Ocean. Over half of the 36 tsunameters in the newly established Indian Ocean Tsunami Warning System, and Adjacent Seas network at that time were damaged during 2006–2010 (Data Buoy Cooperation Panel, 2011). Besides the vandalism issue, high cost is another reason not to implement DART or cabled OBP in tsunami-prone regions worldwide (Bernard and Titov, 2015; González et al., 2005; Mulia and Satake, 2020).

In this study, we explore the potential of establishing a less expensive and island-based tsunami detection network based on a complementary sea-level measuring technique: Global Navigation Satellite System Interferometric Reflectometry (GNSS-IR). The principle of GNSS-IR is to use GNSS satellite signals that reflect off nearby water surface to measure water levels (Larson et al., 2013). These reflected signals interfere with the direct satellite signals, creating measurable interference in the form of an oscillation of the recorded signal-to-noise ratio (SNR) data at low elevation angles. Relative sea level can then be obtained by analyzing the frequency of the SNR oscillation. In the last decade, GNSS-IR technique has been successfully applied in detecting short-term sea-level fluctuations such as storm surges (Peng et al., 2019; Vu et al., 2019; Wang et al., 2022), tsunamis (Larson et al., 2021a), astronomical tides (e.g. Larson et al., 2017; Tabibi et al., 2020), waves (Sepúlveda et al., 2023), seasonal sea-level changes (Peng et al., 2023), and long-term sea-level trends (Peng et al., 2021a) with accuracy comparable to a conventional tide gauge. These pioneering studies demonstrate that coastal GNSS stations can function as conventional tide gauges to measure sea levels with predominant advantages such as simultaneously measuring relative sea-level changes and land-height changes, and importantly rarely to be damaged by extreme sea-level events (Larson et al., 2017, 2021a; Peng et al., 2019; Vu et al., 2019). One limitation of applying GNSS-IR to tsunami detection and source reconstruction is its unequal and low temporal resolution. It is not equally sampled in time and fundamentally limited by the number of satellite overflights and the geometry of the site (Larson et al., 2017). Therefore, GNSS-IR may still face difficulties in detecting short waves with periods of only a few to tens of minutes, e.g., tsunamis (Larson

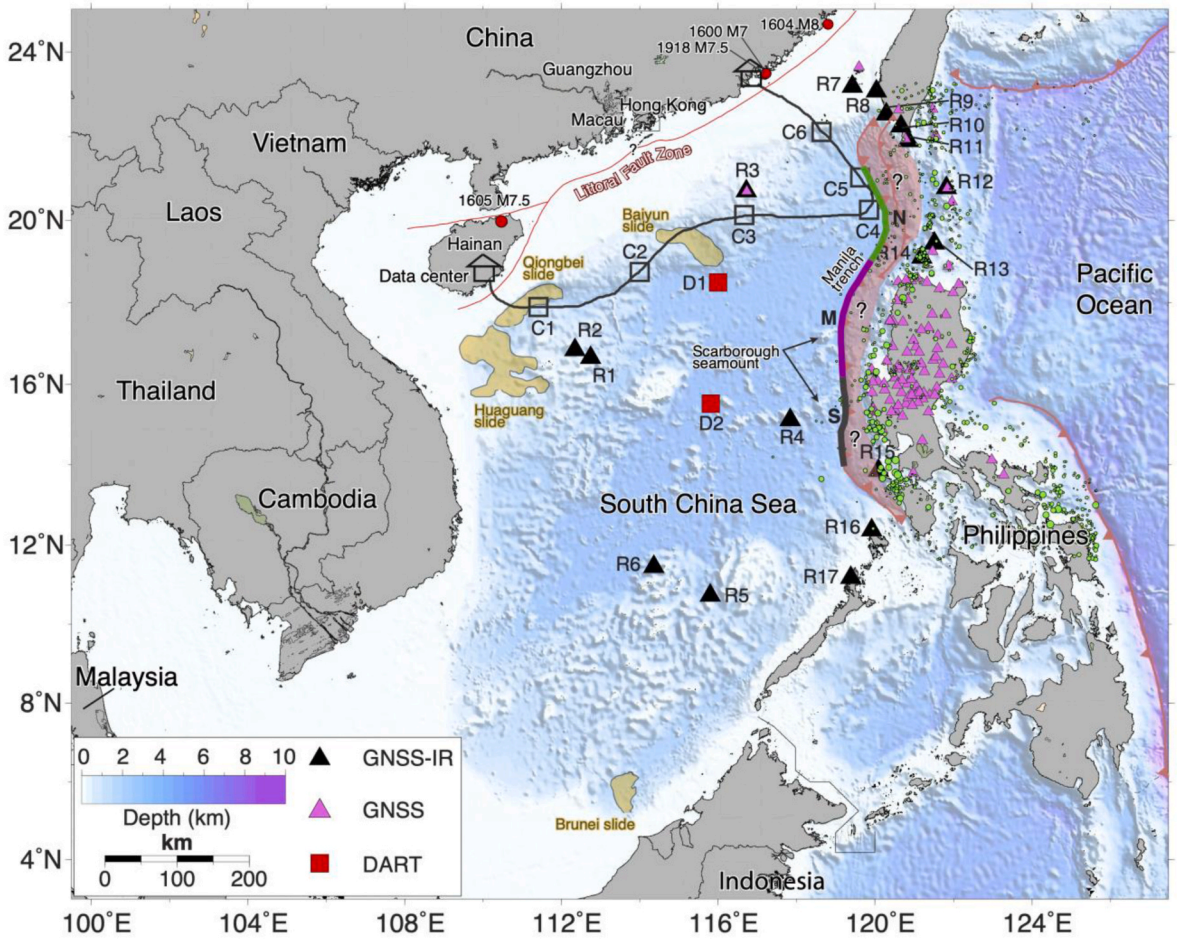

Fig. 1. Tectonic background and potential networks for tsunami detecting and warning in SCS. C1 to C6 are the potential ocean bottom pressure (OBP) wave gauges that would be deployed in the Chinese seafloor cable system; D1 and D2 are the previous deployed DART network (vandalized), and the black triangles are the newly designed GNSS-IR network (R1-R17) in this study. Thick black, pink and green thick lines along the Manila trench indicate the rupture segments that are proposed in Qiu et al., (2019). Green circles show the seismicity with Mw > 5 from the USGS catalog (https://earthquake.usgs.gov/earthquakes/search/). Shaded yellow polygons present the reconstructed spatial extent of the submarine landslides in the SCS region. The landslide boundaries are digitized from (Gee et al., 2007; Sun et al., 2018; Wang et al., 2018).

et al., 2021b). To resolve such sampling resolution issue, we propose a Kalman-filtering approach (Kalman, 1960) that is powerful for assimilating these sparse retrievals from multiple satellite constellations and multiple frequencies to reconstruct an equally sampling (e.g., 1 min) time series like the traditional tide-gauge measurements (Strandberg et al., 2019).

To explore the potential usage of such an island-based GNSS-IR geodetic network for tsunami detection and source reconstruction, we take the SCS as an example region and propose to establish 17 island-based GNSS-IR stations (R1-R17 in Fig. 1) serving as a new tsunami monitoring network. We demonstrate the network's efficacy by comparing its capacity in constraining hypothetic fault slip of typical megathrust earthquakes with other deep-sea monitoring systems. There are three important reasons why we choose the SCS as the application region. Firstly, the densely populated SCS coastlines are exposed to many potential tsunami sources inside the SCS, yet the leading time of tsunami warning is very limited. Confined by the surrounding subducting zones i.e., the Sumatra-Java (to the west and south), the Philippine (to the east) and the Manila (to the northeast) (Li et al., 2021), the SCS basin has developed many complex geological elements that pose a tsunami risk to the populous surrounding coasts (Li et al., 2022; Terry et al., 2017). These elements include the Manila Subduction Zone (MSZ) (Hsu et al., 2016, 2012; Qiu et al., 2019a, b), the submarine landslides at the continental slope region (Gee et al., 2007; Sun et al., 2018; Wang et al., 2018), and the Littoral Fault system in the northern continental shelf of the SCS (Fig. 1) (Li et al., 2022; Xia et al., 2020). Many previous studies suggest that tsunami waves originated from these elements could be devastating, and the time window left for tsunami warning is narrow due to the relatively limited size of the SCS (Li et al., 2019; Liu et al., 2009; Sepúlveda et al., 2019; Yuan et al., 2021; Zhang and Niu, 2020). For tsunamis generated by the Manila subduction zone megathrust earthquakes, the arrival time ranges from ~10 to 30 min for the near source region (i.e., Taiwan and Philippines) to ~2–3 h for southern China or central Vietnam (e.g. Hong Nguyen et al., 2014; Z.-S. Li et al., 2018). Secondly, in the SCS basin, DART buoys have not been in operation in the intermediate to deep water for rapid tsunami detection and warning due to natural or human caused reasons; Thirdly, there are many deep sea islands and reefs distributed inside of the SCS (Fig. 1). The majority of these islands are surrounded by deep water and commonly have narrow shelves with water depth sharply deepened to hundreds to thousands of meters. Such ideal condition ensures that the detected waves follow the linear assumption of shallow water equations, which is suitable for tsunami unit source inversion of the warning system (Li et al., 2016; Liu et al., 2009; Satake and Tanioka, 1999).

We organize the sections as follows. In section 2, we present data and method which includes GNSS-IR technique, Kalman filter and SNR measurements. Since by the time of writing, there is only one successful tsunamis detection using GNSS-IR (Larson et al., 2021b), in section 3, we first demonstrate the performance of a Kalman-filtering approach in reconstructing the 1-min sampling sea-level records from the unequally-sparsely sampled (average 20-min sampling) GNSS-IR sea--level retrievals in the case of storm surge induced by the 2018 Typhoon Mangkut. We also used the GNSS site SC02 at Friday Harbor, Washington State, United States to show that the temporal resolutions of the GNSS-IR sea-level retrievals could be significantly increased after instrumental upgrades. In section 4, we show the effectiveness comparison of the newly designed GNSS-IR network in reconciling hypothetic slip distributions on different segments of the Manila megathrust with previously designed DARTs,and ongoing cabled OBP gauges of the deep-sea monitoring system. In section 5, we discuss the efficiency of GNSS-IR network for tsunami detecting and warning in SCS and its implications for global oceans. Finally, we conclude that the island-based GNSS-IR network is a very promising alternative for tsunami detection, and source reconstruction in oceans where deep-sea monitoring instruments are rare and tsunami potential is high.

2. Data and methods

2.1. GNSS-IR technique

A coastal GNSS station receives both the direct signals, and reflected signals from the nearby sea surface transmitted by satellites. An interference pattern is created when the reflected signals interfere with the direct signals, and is recorded in SNR observables. The pattern can be modeled as a function of the vertical distance between the antenna phase center and the sea surface (Fig. 2a), and the vertical distance can be converted to relative sea level. From the geometry relationship, Larson et al. (2013) show that the frequency of the SNR signal equals to the reflection height (H) devided by the wavelength of the signal. Therefore, one can firstly detrend the SNR signal and, then perform the Lomb-Scargle Periodogram (LSP) to retrieve the frequency. Finally, using the wavelength and LSP determined frequency, we can calcualte the reflection height H or relative sea levels. In addition, the sea-surface height is changing with time, thus a height correction is performed to improve the sea-level retrievals accuracy. Besides, when satellite signals pass through the atmosphere, they are delayed and distorted, causing measurement errors in the SNR signals, and thus unestimates in sea-level retrievals (Peng et al., 2019; Williams and Nievinski, 2017). To deal with such underestimates, astronomical refraction model (Bennett, 1982) and Global Pressure and Temperature 2 Wet (GPT2w) model (Böhm et al., 2015) are applied to correct the elevation angle and sea-level retrivals. Details on how to use the SNR data to derive relative sea levels can be found in Larson et al. (2013) and Peng et al. (2019). This interferometric reflectometry forms the so-called GNSS-IR technique. It is now recognized that the GNSS-IR can serve as a complementary tool to conventional tide gauges to measure sea-level changes (Larson et al., 2013; Peng et al., 2019, 2021b).

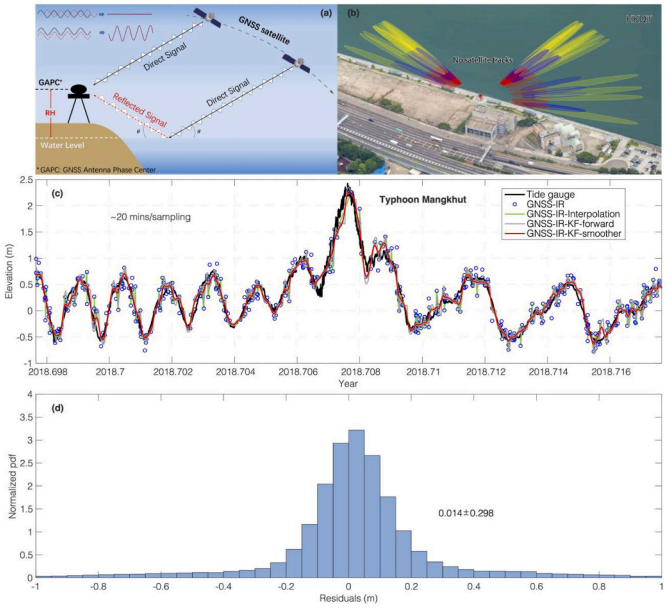

Fig. 2. Conceptual map of GNSS-IR technique, reflection zones and comparison between sea-level change observations and different techniques. (a) schematic diagram representation of the reflected GNSS signal geometry. RH is the height between the phase center of the GNSS antenna and the reflection water surface level. (b) location and Fresnel zone of the GNSS site at Hong Kong. Colored regions show the GNSS-IR reflection zones for L5 frequency of the GPS constellation (see 2.2). (c) sea-level measurements comparison between tide gauge (1-min sampling), GNSS-IR approach (~ average 20-min sampling), interpolation and GNSS-IR-based Kalman filtering (GNSS-IR-KF-forward, GNSS-IR-KF-smoother) technique (1-min sampling). (d) sea-level variation residuals (between the tide gauge measurements and GNSS-IR-KF-smoother results) distribution with numbers showing the mean and standard deviation.

Besides site geometry (determining the zone of water area that the GNSS antenna can sense), the temporal resolution of GNSS-IR sea-level measurements also depends on the number of satellites overflights; a better temporal resolution can, therefore, be expected if the GNSS receiver can receive satellite signals from multiple constellations such as BeiDou (BDS), Global Positioning System (GPS), GLONASS, Galileo, IRNSS, QZSS etc (Figs. 3 and 4). This is crucial for capturing short-term extreme sea-level events. For example, multi-constellation GNSS-IR successfully detected the recent extreme sea-level variation events i.e., Hurricane Laura and seismic-triggered tsunamis events (Larson et al., 2021a; Wang et al., 2022). However, due to the nature of the GNSS-IR technique, sea-level retrievals are irregularly sampled in time. If further limited by the number of satellite overflights, and the geometry of the site, GNSS-IR sea-level measurements could look like an unequally down-sampled time series as compared with uniformly sampled tide-gauge records (Figs. 2c, 3 and 4). Despite the successful examples, a down-sampled time series could miss the high-stand peaky sea levels, which cannot be used directly either in analysis or interpretation especially for short-term extreme sea-level events i.e., storm surges and tsunamis. Although these sparse measurements are unequally distributed, they carry the sea-level information at that time epoch. If a certain technique that can predict future information based on previous measurements (sparse measurements), and use the new (next sparse measurements) to update the predicted sea levels whenever there is new measurement available, then the sparse-irregular GNSS-IR sea-level retrievals are valuable for reconstructing a denser time series that has the minute-sampling rate as tide-gauge records. This is where the Kalman filter comes into play.

2.2. Kalman filter

The Kalman filter is a powerful technique that is widely used in data assimilation. The filter affords the optimized solution for model parameters based on the noisy measurements (Kalman, 1960). It performs the filtering process in two sequential steps. The first is the prediction step which has a system matrix (F) that describes how the model parameters are physically correlated (Eq. (1)). The second is the updating step which has an observational matrix (H) that connects the model parameters to the measurements (Eqs. (2) and (5)). In doing so, the filter predicts the model parameters based on the system matrix, and previous measurements for next new time epoch (Eqs. (1)–(4)), and then update these values by incorporating the measurements if there are any measurements available at this new time epoch (Eq. (5)). If these measurements are sampled at different time epochs, the filter will assimilate them each by each in a sequential manner. If there were data gaps, then the filter predicts model parameter values based on the system matrix and previous measurements (Eqs. (3) and (4)), and thus fills up these data gaps with the predicted values. Therefore, the filter is powerful to integrate multiple sea-level retrievals measured at arbitrary time epoch from various satellite constellations. In this framework, the filter can reconstruct the time series with the same time-interval as the co-located tide gauge; thus, the filtered time series can be used for detailed data analysis, and interpretation for extreme sea-level events such as storm surges and tsunamis. The Kalman filtering process is given by equations (1)–(5) as follows.

$$x_k = F_{k-1}x_{k-1} + \omega_{k-1} \tag{1}$$

$$y_k = H_k x_k + \gamma_k \tag{2}$$

$$\omega_k \sim (0, Q_k)$$

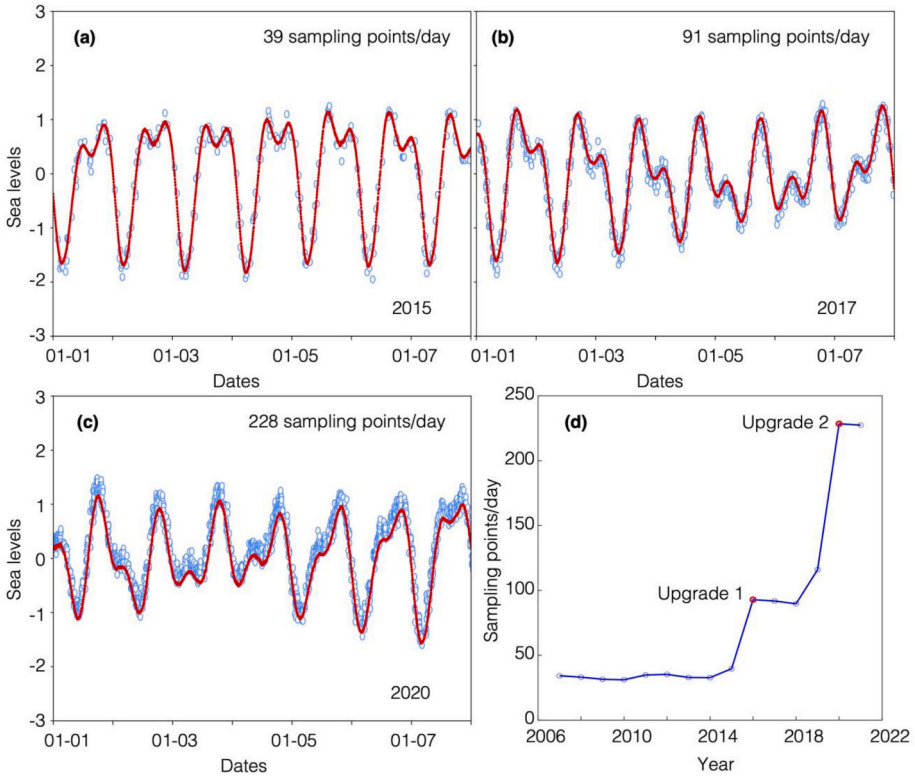

Fig. 3. An increasing in temporal-sampling of sea-level retrivals example at GNSS site SC02 in the US retrieved by GNSS-IR technique. a) to (c) show a 7-day time series of sea-level retrievals in Jan 01–08 of the year 2015, 2017 and 2020, indicating the sampling rate per day have been increasing constantly with the instrument upgrading as multiple satellite constellation and frequency are captured by the GNSS receiver. (d) shows an exponential-increasing trend in the average sea-level retrievals sampling rates per day in the past 15 years at site SC02. The two instrumental upgrades are highlighted. The full 15-year sea-level retrievals is shown in Fig. S2.

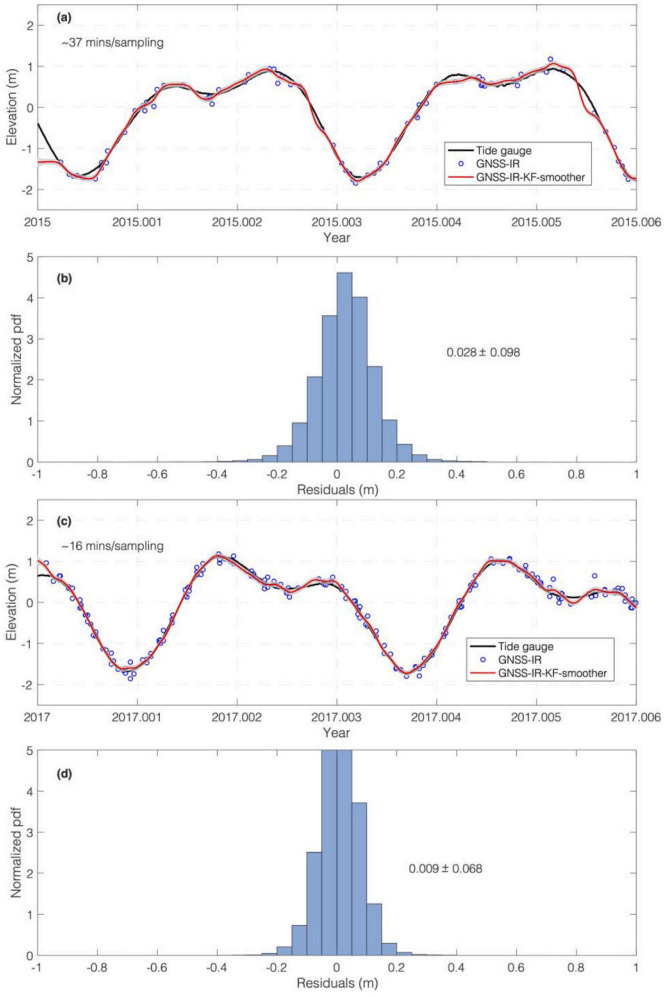

Fig. 4. A detailed view of sea-level variation example (~2 days) at SC02 GNSS site retrieved by GNSS-IR technique and it's comparison between the smoothed Kalman-filter results and the co-located tide gauge. a) shows the first 2-day retrieved relative sea-level heights and the Kalman filtering (gray shaded area show the uncertainty estimates) results in January 2015; b) shows the residual (between the Kalman filtering results and the tide gauge shown in (a)) distribution with numbers showing the mean and standard deviation; c) shows the retrieved first 2-day relative sea-level heights and Kalman filtering (gray shaded area show the uncertainty estimates) results after the instrumental upgrade in January 2017; d) shows the residual (between the tide gauge measurements in (c) and Kalman filtering results) distribution with numbers showing the mean and standard deviation.

$$\gamma_k \sim (0, R_k)$$

$$P_k^- = F_{k-1} P_{k-1}^+ F_{k-1}^T + Q_{k-1}$$

$$K_k = P_k^{-1} H_k^T \left(H_k P_k^{-1} H_k^T + R_k\right)^{-1} \quad (3)$$

$$x_k^- = F_{k-1} x_{k-1}^+ \quad (4)$$

$$x_k^+ = x_k^- + K_k \left(y_k - H_k x_k^-\right) \quad (5)$$

$$P_k^+ = (I - K_k H_k) P_k^-$$

Where k represents the current time epoch, x_k is the model parameters which are the sea-level retrieval, and its rate at time step k, F_{k-1} is the system or transition matrix which is $\begin{bmatrix} 1 & dt \\ 0 & 1 \end{bmatrix}$, dt is the time step; ω_{k-1} (model parameters) and γ_{k-1} (measurement) are white noise processes, zero-mean, uncorrelated, and have known covariance matrix $Q_k = \begin{bmatrix} \alpha_1^2 dt & 0 \\ 0 & \alpha_2^2 dt \end{bmatrix}$, $R_k = \delta_y^2$, respectively. H_k is the measurement matrix, P_{k-1}^+ is the measurement-updated covariance matrix of the model parameters at time step $k-1$, P_k^{-1} is the covariance matrix prediction for time step k, x_{k-1}^+ is the filtered model parameters results at time step $k-1$, x_k^- is the predicted model parameters at time step k, x_k^+ is the measurement-updated model parameter estimates at time step k. In addition to such filtering process forward in time, we also apply the Rauch-Tung-Striebel (RTS) smoother which uses the forward estimates to smooth the model parameters backward in time, resulting in smoothed outlier-free estimates (RAUCH et al., 1965).

In the following sections, we will use the sea-level retrievals at the GNSS receivers named HKQT, SC02 and their co-located tide gauges to demonstrate how the Kalman filter performs in comparsion with tide-gauge measurements (Figs. 2–4).

2.3. SNR measurements at GNSS site HKQT and SC02

The HKQT GNSS station was installed at the rooftop of a building close to Quarry Bay at Hong Kong (Fig. 2b). This site is equipped with a Trimble NetR9 receiver, and a TRM59800 antenna; and the receiver is configured to receive signals from GPS and GLONASS satellites. We downloaded the GNSS data in RINEX3 (Receiver Independent Exchange version 3) format with a sampling rate of 5 s over the period of 2016–2020 from the SMO (Survey and Mapping Office, https://www.geodetic.gov.hk/en/index.htm) of Hong Kong Lands Department. After a detailed investigation of the Fresnel zone (Fig. 2b), we find that the elevation angle ranging between 4° and 9°, and the azimuth ranging between −60°~105° could capture the reflected signals for sea-level retrievals (Fig. 2 b and c). We used the GNSS reflection software gnssref (Roesler and Larson, 2018) to perform the sea-level retrievals. To obtain sea-level retrievals at the best possible temporal resolution and accuracy, we used GPS SNR data at L1 and L5 frequencies and GLONASS SNR data at L1 and L2 frequencies. Errors due to tropospheric delay and height rate change over a satellite pass ($\dot{H}$) were corrected by using the algorithm proposed by Larson et al. (2013). For validation, we downloaded independent sea-level measurements with a sampling rate of 1-min from a co-located tide gauge Quarry Bay during the same period from the IOC website (Data statement). Comparison of relative sea-level retrievals from GNSS-IR, GNSS-IR Kalman filtering results, and the tide-gauge measurements are shown in Fig. 2c and d and S1.

The SC02 GNSS station at Friday Harbor was initially installed in 2001 by the Pacific Northwest Geodetic Array (http://www.geodesy.cwu.edu/). The antenna has been upgraded in 2006 and 2015. The 2015 upgrade started allowing multi-GNSS signals, i.e., GPS L1, L2, L5, GLONASS L1 and L2 frequencies, and Galileo at E1, E5a, E5b, E5 frequencies to be received in November 2019. The 15-s sampling rate GNSS data of SC02 in RINEX2 format are downloaded from UNAVCO (https://data.unavco.org/). We search the signals with an elevation angle between 5°~13°, and azimuth angle between 50°~240° for maximizing sea-level retrievals at SC02. We obtain the reflection height is 3 m–12 m and peak-to-noise ratio >3 with spectral peak value > 6 for all 9 GNSS signal frequencies (Fig. 3 and S2). The bias caused by tropospheric delay, and the sea-level height variations over a satellite pass ($\dot{H}$) are corrected by using the approach from Larson et al. (2013). A tide gauge at Friday Harbor, locates ~345 m away from the GNSS SC02 station. This tide gauge is monitored, and maintained by the Center for Operational Oceanographic Products and Services (CO-OPS) of the U.S. National Oceanic and Atmospheric Administration (NOAA), and provides continuous data on monitoring sea-level variations. Tide gauge time series data with a 6-min sampling rate are retrieved from the National Ocean Service website (http://tidesandcurrents.noaa.gov/) of NOAA. Comparison of relative sea-level retrievals from GNSS-IR, GNSS-IR

Kalman filtering results, and the tide-gauge measurements are shown in Figs. 3 and 4, S2, S3, S4 and S5.

3. Effectiveness of kalman filtering approach

We first present the Kalman filtering results based on the coarser sea-level retrievals from the GNSS-IR site HKQT. This site captures the entire storm surge process when the extreme 2018 Typhoon Mangkhut swept the southern coast of China. Then, we present the sea-level retrievals and Kalman filtering results for example time periods of GNSS-IR site SC02. This site has a long-term sea-level measurements since 2007, and it has experienced several equipment upgrades since 2015, which allows us to compare the variations of temporal-resolution when different satellites of multiple constellations are involved.

3.1. GNSS-IR sea-level retrievals and kalman filtering at HKQT

During filering process, we performed many experiments, and found $\alpha_1 = 3.16e^{-3}, \alpha_2 = 3.16e^{-4}$ in the covariance matrix Q_k that can best capture the curvature of the sea-level variations while simultaneously smoothing out the outliers (Fig. 2c). Fig. 2c shows the comparison between the GNSS-IR sea-level retrievals from the HKQT station, the co-located tide-gauge observation, and the GNSS-IR Kalman filtering results. In general, sea-level retrievals agree well with tide-gauge measurements. Although two GNSS satellite constellations, and their dual-frequency signals were incorporated into the sea-level height retrievals, the unequal-sampled heights remain sparse (on average, ~20 min/sampling) as comparing with the 1-min sampling tide gauge measurements (Fig. 2c). Even so, the sparse retrievals capture the temporal pattern of sea level well, especially the extreme sea-level variation during the typhoon Mangkhut (Fig. 2c). Since sea-level retrievals are sparsely and unequally determined, it is not straightforward to directly compare with the 1-min sampling tide-gauge observations. Conventionally, one could interpolate, that will introduce bias from the imperfect retrievals (e.g., outliers, Fig. 2c). The Kalman-filtering approach uses these sparse measurements to perform prediction, updating forward filtering process and backward RTS smoother, which results in a 1-min sampling interval sea-level measurements that have a compariable amplide with the 1-min sampling tide-gauge measurements (Fig. 2d).

3.2. GNSS-IR sea-level retrievals and kalman filtering at SC02

The accuracy of the Kalman filtering results can be largely improved when more sea-level retrievals (higher sampling) from multiple satellite constellations and frequencies (Larson et al., 2021a) are used. Indeed, the SC02 site provides an excellent example of how sampling capabilities can be significantly improved. In 2015, the averaging sampling is 39 measurements per day equivalent to ~37 min/sample (Fig. 3). When upgraded to multi-GNSS receiver, the sampling rates almost tripled in 2017, and further increased by 6–7 times in 2020. The average temporal resolutions have been densified to ~16 min and ~6 min, respectively (Fig. 3 and S2).

Based on these sea-level retrievals, we use Kalman filter to get the filtered results that have the same time sampling rate with the collocated tide gauge (6-min sampling). We performed several rounds of experiments when filtering the GNSS-IR sea-level retrivals. We find that $\alpha_1 = 3.2e^{-3}, \alpha_2 = 1e^{-3}$ of the covariance matrix Q_k that can capture the sea-level variation and filter out the outerliers, resulting in small mean and standard deviation compared with the tide gauge measurements (Fig. 4). However, there are some deviation, which could be introduced by local signals or geometry effect of the multiple satellite constellations (Fig. 3, S2, S3 and S4). The comparison suggests that increasing in temporal resolution of the GNSS-IR retrievals results in a significant error reduction in Kalman filter estimates (Fig. 4 and S5). In fact, the Kalman filter not only regularizes the sparse-irregular samples to generate an equal-temporal sampling of the retrievals, but also significantly improves its accuracy by smoothing out the outliers (Figs. 2c and 4).

3.3. Kalman filtering validation with tsunami measurements of the 2011 Tohoku-Oki event

To further demonstrate the effectiveness of the Kalman filter on processing real tsunami waves, we selected tsunami waveforms generated by the 2011 Mw 9.1 Tohoku-Oki earthquake to perform sensitivity tests. We used tsunami waveforms recorded by two representative stations in offshore Japan: GPS buoys (TM1) and DART (21418) as examples (Fig. 5). We first downsampled the temporal resolution by randomly removing some measurement points. In doing so, we can fully test whether the filter can reconstruct the tsunami waveform from a coarse-unequal sampled measurements. The results demonstrate that the filter could recover the waveforms with sufficient similarity to the initial records (Fig. 5).

In our examples, signals from GPS, GLONASS and Galileo signals were used. If the instrument is further upgraded to receive signals from other constellations, such as, BeiDou, IRNSS, and QZSS, a better temporal resolution of GNSS-IR sea-level measurements can be expected. Combined with the Kalman filter approach, this would allow us to detect centimeter or sub-centimeter sea-level variations from minutes to hourly, daily, and long-term timescales. In addition, the two stations (HKQT and SC02) are primarily for positioning related purposes; therefore, geodetic-quality GNSS receivers, and antennas with a cost > US$10,000 were used. To ensure reliable positioning, their antennas are zenith-pointing, which suppress reflections. Recently, Karegar et al. (2022) demonstrated that a customized GNSS-IR senor with the antenna being oriented toward the water body not only has far superior reflection characteristics to improve temporal resolution and accuracy, but also significantly reduces the cost to < US$150. Although such design will result in poor positioning capabilities, it could be potentially useful for a flood, and tsunamis early-warning system as it is low-cost, high--precision, and technically accessible worldwide. However, the challenge of using either geodetic-quality or low-cost GNSS-IR equipment for tsunamis warning is its real-time monitoring capacity. In fact, using station GTGU at the Onsala Space Observatory, Sweden, Strandberg et al. (2019) demonstrated that combining inverse modelling of reflection data with a Kalman filter approach, it is technically possible to use GNSS-IR to monitor real-time sea levels. With recent application of the GNSS real-time processing used for earthquake warning (e.g. Chen et al., 2020; Williamson et al., 2020), an integration of GNSS-IR sea-level measurements and GNSS displacements based unit source inversion scheme for real-time tsunami warning is possible.

In summary, the combination of GNSS-IR and Kalman-filtering techniques enable the filtered 1-min sampling sea-level heights that can capture tsunami waves with periods of several minutes, which can be used for tsunami detecting, warning and source reconstruction.

4. Evaluation of potential GNSS-IR network for tsunami warning in the SCS

To domanstrate the effectiveness and efficiency of the proposed GNSS-IR network, we first design an island-based GNSS-IR gendetic network in the SCS (R1-R17 in Fig. 1). We then build a tsunami unit source inversion scheme specifically for megathrust earthquakes originated from the MSZ. Finally, we compare the network's capacity in constraining the slip distribution on the Manila megathrust with that of the previously designed DARTs (D1, D2 in Fig. 1), and possible OBP gauges mounted on on-going seafloor cable deployment (black open squares C1–C6 in Fig. 1). China has an on-going project which will deploy a seafloor observational cable system in the SCS to conduct comprehensive multidisciplinary marine observations (Fig. 1). The

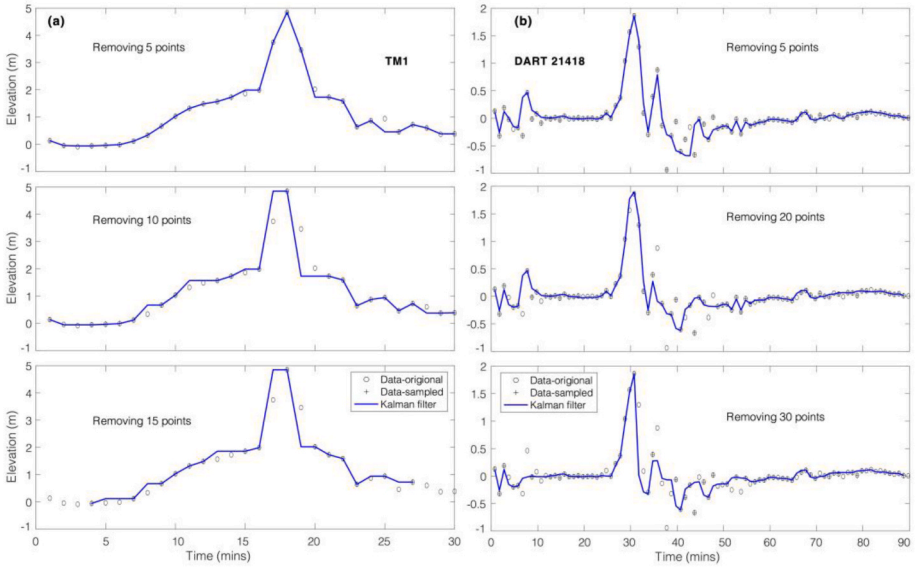

Fig. 5. Kalman filter validation with real tsunami measurements at TM1 and DART 21418 following the 2011 Mw 9.1 Tohoku-Oki earthquake. (a) upper panel: filtered results by randomly removing 5 measurement points; middle panel: filtered results by randomly removing 10 measurement points; lower panel: filtered results by randomly removing 15 measurement points. (b) same with (a) for DART 21418.

project started in 2015, and the whole system aims to be completed in 2026. The cable starts at the southeastern coast of Hainan province and runs along the continental slope all the way to the Luzon Strait and ends at a coastal city, Shantou (Fig. 1). Along the cable, there are 6 nodes that can deploy multiple sensors including the OBP gauges. In this framework, we setup an OBP gauge (open squares) at each node, and then evaluate its capacity in tsunami detection (Fig. 1).

4.1. An island-based GNSS-IR geodetic network in the SCS

In order to locate the GNSS-IR station in an ideal location to effectively detect tsunami waves from MSZ, we use hypothetical earthquake scenarios at the MSZ to find their ideal locations. Taking advantage of the widely distributed islands, and reefs in the SCS region, we propose to install 17 coastal GNSS stations (black triangles R1-R17 in Fig. 1). The spatial distribution of the GNSS sites is inspired by the tsunami energy distribution generated by hypothetic earthquakes originated from the MSZ (Qiu et al., 2019a, b). Because the maximum energy distribution of tsunami waves is influenced by the earthquake rupture orientation, and the seafloor bathymetry along the propagation path (Li et al., 2022; Qiu et al., 2019b). In this case, station R7 to R13 well capture the waves initiated from the northern segment (N) of the MSZ. The largest unknown is whether the Manila trench will rupture as a whole in a giant Mw 9 earthquake (Megawati et al., 2009) or as great earthquake (Mw > 8) in separate segment remains challenging to predict (Qiu et al., 2019a, b). On the other hand, global subduction-zone study reveals that geological barriers or sharp geometry variation along fault strike e.g., bending will likely develop discontinunities that hinder rupture propagation, resulting in rupture segments (Philibosian and Meltzner, 2020). As the prevalence of large-scale Scarborough seamounts (Fig. 1), and also the significant fault bending along the Manila trench, we follow Qiu et al., 2019a, b to consider segmental-rupture scenarios (Fig. 1). In this framework, we consider as many stations as possible along the hypothetical tsunami propagation path in each rupture segment, and complement some stations in the rest directions to compose an array that can capture the impact of tsunami waves. Thus, station R1 to R3 mainly capture waves from the middle segment (M), and R4 to R6 and R16 to R17 mainly capture waves from the southern segment (S) (Fig. 1). We consider it is plausible to install GNSS-IR sites at these locations. The GNSS-IR stations preferably should be deployed at the coast area facing incoming tsunami waves if possible. As suggested by previous studies, the first incoming tsunami waves may maximumly carry the source information and less modulated by local bathymetry effect (e.g. Y Y Wang et al., 2021). So when such incoming waves are used for earthquake source inversion, the uncertainties associated with bathymetric effect could be minimized. The stations will be installed near the coast with a height that allows the reflection zone (approximated as the First Fresnel Zone, Fig. 2b and S6) (Larson et al., 2013) to cover water areas with depth >10–20 m. Such water depth ensures that the detected waves follow the linear assumption of shallow water equations, thus suitable for tsunami unit source inversion of the warning system (Li et al., 2016; Liu et al., 2009; Satake and Tanioka, 1999).

4.2. Tsunami unit source inversion

We used the triangular mesh to discretize the megathrust fault, which can capture the large structural variation of the Manila megathrust better, and thus could improve the model prediction on the seafloor displacement, and hereafter the tsunami wave dynamics (Qiu et al., 2019b). With the mesh, we computed the dip-component tsunami-wave Green's functions at each gauge (GNSS-IR, OBP cable nodes and DARTs, Fig. 1) for each triangular element, by using the Cornell Multi-grid Coupled Tsunami model (COMCOT, Liu et al., 1995; Wang and Liu, 2006). We do not compute the strike-component tsunami-wave Green's functions, as it will be easily calculated and assimilated in the unit source inversion if needed in real cases. The COMCOT software has been well-benchmarked, and been widely used in tsunami science in the past decades (Power et al., 2012; Wang and Liu, 2007).

We assemble these tsunami-wave Green's functions, and the displacements from onshore GNSS sites to conduct the tsunami unit source joint inversion by using the linear-inversion scheme proposed by Satake and Tanioka (1999). We first create the hypothetic earthquake model (slip) in each segment of the MSZ (Figs. 6–8, zones 1–3 in Qiu et al., 2019a, b). These models essentially mimic the large slip amplitude at shallow megathrust that could occur in i.e., tsunami earthquake (Hill et al., 2012) or trench-breaking ruptures (Satake et al., 2013) as a consideration of worst-case scenario for an equal-moment seismogenic earthquake (Figs. 6–8). Then each model predicts ground displacements at the onshore GNSS sites, and the corresponding tsunami waveforms at each wave gauge of each network (Fig. 1). These waveforms and

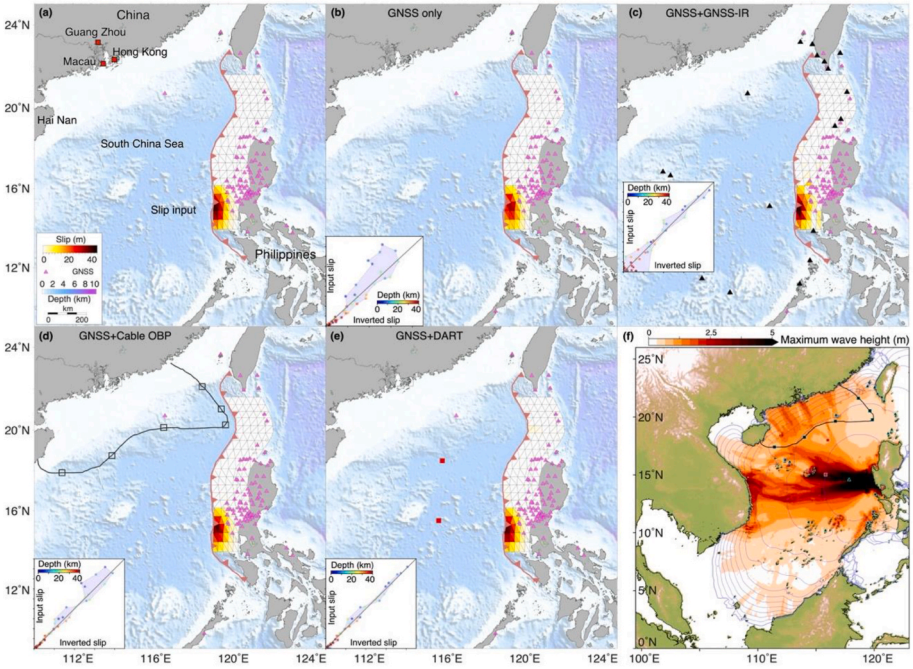

Fig. 6. Efficiency tests for reconstructing the hypothetical slip model in the southern segment of the Manila subduction zone (Fig. 1) when implementing different networks. (a) the hypothetical slip model; (b) the reconstructed slip model using the onshore GNSS sites; (c) the reconstructed slip model using the onshore GNSS sites and GNSS-IR network; (d) the reconstructed slip model using the onshore GNSS sites and the seafloor cable OBP network; (e) the reconstructed slip model using the on shore GNSS sites and the previous DART network; (f) presents the maximum wave amplitude in the SCS from the slip input model in (a), with blue contours showing the arrival time at a 30-min interval. In (b) to (e), the inset maps show the hypothetical input slips verse the inverted slips with colors showing the depth information. If the network can perfectly reconstruct the slip input, then the colored stars will align on the black line, otherwise they scatter around the line.

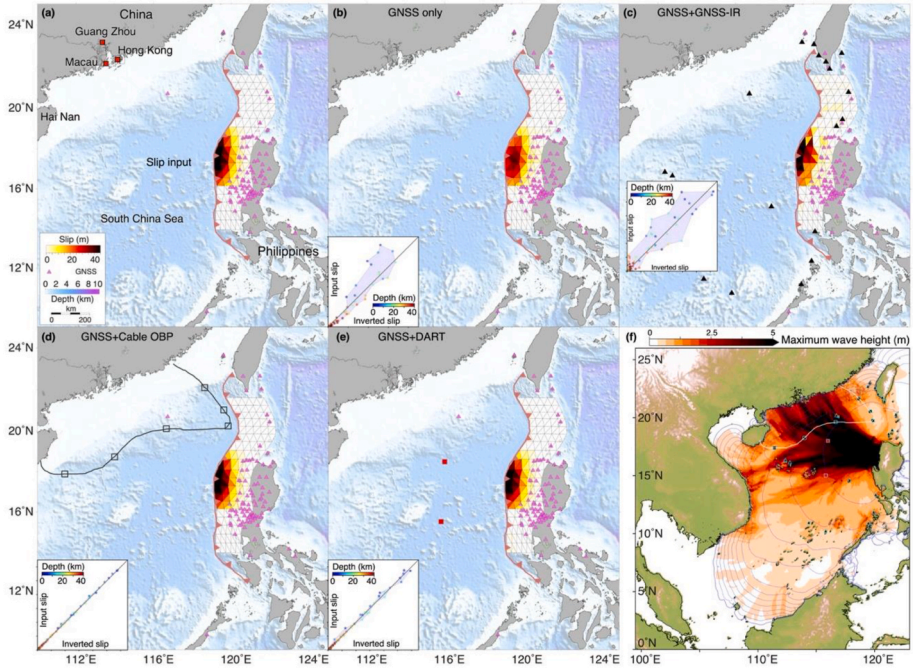

Fig. 7. Efficiency tests for reconstructing the hypothetical slip model in the middle segment of the Manila subduction zone (Fig. 1) when implementing different networks. (a) the hypothetical slip model; (b) the reconstructed slip model using the onshore GNSS sites; (c) the reconstructed slip model using the onshore GNSS sites and GNSS-IR network; (d) the reconstructed slip model using the onshore GNSS sites and the seafloor cable OBP network; (e) the reconstructed slip model using the on shore GNSS sites and the previous DART network; (f) presents the maximum wave amplitude in the SCS from the slip input model in (a), with blue contours showing the arrival time at a 30-min interval. In (b) to (e), the inset maps show the hypothetical input slips verse the inverted slips with colors showing the slipped depth information. If the network can perfectly reconstruct the slip input, then the colored stars will align on the black line, otherwise they scatter around the line.

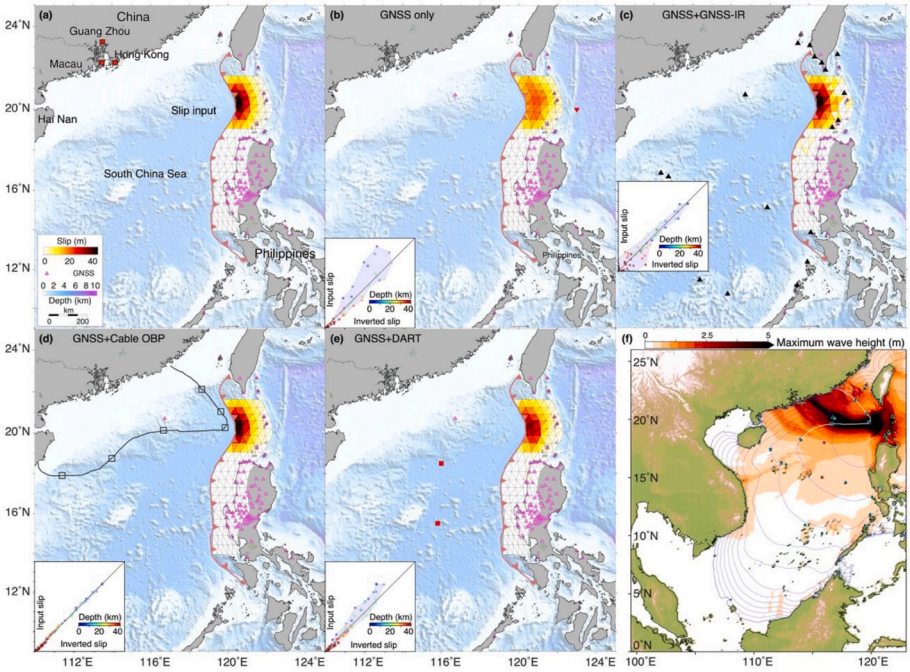

Fig. 8. Efficiency tests for reconstructing the hypothetical slip model in the northern segment of the Manila subduction zone (Fig. 1) when implementing different networks. (a) the hypothetical slip model; (b) the reconstructed slip model using the onshore GNSS sites; (c) the reconstructed slip model using the onshore GNSS sites and GNSS-IR network; (d) the reconstructed slip model using the onshore GNSS sites and the seafloor cable OBP network; (e) the reconstructed slip model using the on shore GNSS sites and the previous DART network; (f) presents the maximum wave amplitude in the SCS from the slip input model in (a), with blue contours showing the arrival time at a 30-min interval. In (b) to (e), the inset maps show the hypothetical input slips verse the inverted slips with colors showing the slipped depth information. If the network can perfectly reconstruct the slip input, then the colored stars will align on the black line, otherwise they scatter around the line.

displacements are used as synthetic data for efficiency tests of each wave gauge network (i.e., GNSS-IR, DARTs and cable-based OBP gauges, Fig. 1). Finally, with these pre-computed tsunami-wave Green's functions and displacements, we jointly invert these synthetic data for the distributed slip on the megathrust fault. To avoid over fitting the synthetic data (Fig. S7), we used the stress kernel to regularize the spatial gradient in slip on the fault following previous studies (Qiu et al., 2019a, b; Yang et al., 2022). A smoothing parameter that controls the gradient is determined by the simple trial-and-error approach. In doing so, we obtain the optimized slip distribution based on the observational network. The obtained slip model is compared with the hypothetical slip (Figs. 6–8, inset maps) to define its efficiency in tsunami detection and earthquake source reconstruction.

4.3. Earthquake source reconstruction in the southern MSZ

Fig. 6a shows the hypothetical slip model for the southern segment of the Manila trench, which has a seismic moment magnitude equivalent to Mw 8.7. The inset maps show hypothetical slip amplitude inputs verses inverted slip amplitudes with colors showing the depth information. If a network can perfectly reconstruct the slip input, then the colored stars align on the black line. When only the onshore GNSS sites were used in the inversion, the inverted slip amplitudes are significantly smaller than the hypothetical slip values at all depths (0–40 km) due to the lack of constraint from the seafloor measurements (Fig. 6b, inset map). The inverted model, in turn will underpredict the tsunami wave amplitudes along the coasts in the SCS. This issue is largely improved when offshore wave gauges are incorporated in the inversion (Fig. 6 c, d, and e). When DARTs are included, the inverted slip amplitudes are commensurate with the hypothetical slip amplitudes except the intermediate depth region (~20–30 km) (Fig. 6e). As the cable-based OBP gauges are located outside of the main energy-propagation path (Fig. 6f), slip model constrained by such gauges and onshore GNSS data significantly underestimates the intermediate and shallow slip amplitudes, although the small-amplitude slip at deep depths (>30 km) are better determined (Fig. 6d, inset map). If the GNSS-IR network is incorporated in the inversion, the slip amplitude at shallow and intermediate depths (<20 km) are better reconciled than that at the deep-depth (>20 km) (Fig. 6c, inset map). Although the deep-depth slip amplitudes are underestimated, they are small, and thus contribute minor tsunamis hazard. In sum, similar to the DARTs, the GNSS-IR network performs well in constraining the megathrust slip distribution and amplitude and in detecting tsunamis, playing an important role in reconstructing the earthquake source.

4.4. Earthquake source reconstruction in the middle MSZ

In this segment, the hypothetical slip model is shown in Fig. 7a which has a seismic moment magnitude equivalent to Mw 8.9. Similar to the issue with the southern segment, if only the onshore GNSS sites are used in the inversion, the inverted slip amplitudes are largely underestimated at all depths (0–40 km) (Fig. 7b). As expected, if wave gauges such as DARTs or cable-based OBP gauges were incorporated in the inversion, the slip amplitudes are recovered remarkably well or almost perfectly determined (Fig. 7 d and e, inset map). This is because the location of the gauges is well located in the main propagation path of the tsunamis (Fig. 7f). For the GNSS-IR network, as few islands seat outside of the tsunami propagation path (Fig. 7f), the efficiency in detecting tsunami waves is slightly worse than that of both the DARTs and OBP networks, but it still captures the general slip pattern well (Fig. 7c). In summary, the cable-based OBP, and the DARTs perform equally well in determining the slip distribution on the megathrust. The GNSS-IR network underestimates some intermediate to shallow slip values, but can still reconcile the first-order slip pattern very well, which is crucial to predict accurate tsunami arrival time and first-order tsunami wave heights along the southern coast of China during early warning.

4.5. Earthquake source reconstruction in the northern MSZ

We show the hypothetical earthquake model with an equivalent seismic moment magnitude Mw 8.8 in Fig. 8a. In the inversion, the onshore sparse GNSS sites poorly constrain the distributed slip on the megathrust, which underestimates almost twice of the slip maxima, and mislocates the maximum slip locus as comparing with the hypothetical slip model (Fig. 8b). Therefore, the inverted slip model (Fig. 8b) will predict lower tsunami amplitudes and incorrect tsunami arrival times in the SCS. These prediction issues are significantly improved when offshore wave gauges are assimilated in the inversion (Fig. 8d and e). The cable-based OBP does well in reconstructing the slip amplitudes and pattern, and thus importantly for tsunami warning (Fig. 8d). While the DARTs do poorly in slip distribution reconstruction, and tsunami detection (Fig. 8e), because their locations are out of the tsunami energy dissipation path (Fig. 8f). For the GNSS-IR network, in general, it estimates commeasurable slip amplitudes from intermediate to shallow depths on the megathrust as comparing with the hypothetical slip amplitudes (Fig. 8c, inset map), which claims for the amplified tsunami hazard along the coasts in the SCS (Lay, 2018; Qiu and Barbot, 2022). In sum, the cable-based OBP works quite well in reconstruction of slip distribution on the megathrust, while the DARTs can only reconcile the general slip pattern, and largely underestimate the slip amplitudes. Finally, the GNSS-IR network can efficiently reconcile the slip maxima and pattern, which are the key parameters for a timely forecast of the arrival times and amplitudes of tsunami waves in the early warning.

5. Discussion

5.1. Examine the efficiency of GNSS-IR network for tsunami detecting and warning in the SCS

Our newly proposed GNSS-IR network, and Kalman filter approach provide the basis for building a unit source slip inversion scheme in the SCS that could serve as a complementary network to the existing tsunami detecting and warning system. Through our inversion tests, we conclude that the constraint afforded by onshore GNSS sites only is weak for slip amplitudes estimates of the shallow megathrust earthquakes, which will, in turn, improperly forecast the tsunami wave characteristics. The locations of the conventional DARTs offer tight constraints to the distributed slip on the megathrust initiated either in the southern and central segment, yet a slightly loose constraint to that of northern segment of the MSZ (Figs. 6–8). Moving both DARTs northeastward to locations closer to the trench could provide better constraint on fault slip originated from all three segments, as suggested by An et al. (2018). With future deployment of OBP gauges on the seafloor cable system in the northern SCS basin, they can largely improve the constraints of slip distribution on the megathrust, especially for the middle and northern segments of the MSZ (Figs. 6–8). The proposed islands-based coastal GNSS-IR network not only can efficiently reconstruct the slip distribution on the Manila megathrust, but also runs with a much lower risk of vandalism. As suggested from all the inversion tests and comparisons between different networks, it is the GNSS-IR network that can reconcile the slip amplitudes and patterns sufficiently well at all segments of the MSZ for a given hypothetical earthquake (Figs. 6c, 7c and 8c). Such well reconciled slip pattern and amplitudes afford crucial information for tsunami forecasting along the coasts in the SCS during the warning stage.

To further examine and compare the efficiency of each network, we take the possible earthquake scenario in the northern segment as a demonstration case. Tsunamis triggered by this segment (Zone 3 in Qiu et al. (2019b)) of the MSZ pose significant threat to the southern coast of China (Li et al., 2016; Qiu et al., 2019b; Yuan et al., 2021). Part of the reason is because the tsunami waves adjust the propagation direction at the continental slope region in the northern continental slope of the SCS due to the refraction effect, directing tsunami energy towards Hong Kong and Macau in the Greater Bay area (Fig. 8f) (L. Li et al., 2018a; Li et al., 2022). We define the network efficiency by comparing the slip model improvements when more stations are involved in the inversion. We use a performance index number, which is calculated based on the data and model residuals, to describe the efficiency. The smaller index corresponds to a higher efficiency (Fig. 9). Within the first 30 min after the earthquake, the cable-based OBP and GNSS-IR networks can reconstruct a comparable slip distribution on the megathrust, similar to the hypothetical slip model (Fig. 9 a, b and d). It requires, however, nearly 60 min before the previously designed DARTs stations could detect the first tsunami leading waves (Fig. S8). Moreover, assimilating their records to the source inversion does not constrain the distributed slip well (Fig. 8e and S8). As time goes, for both the cable-based OBP and GNSS-IR networks, the improvement of inverted slip distributions is trivial when tsunamis propagate after 60–90 min, indicating that the slip distribution could be stably and accurately resolved by the cabled OBP and GNSS-IR networks within half an hour after the quake (Fig. 9). These early well-determined slip models (Fig. 8 a and d) can be further used as an input for tsunami warning center to rapidly forecast the tsunami waves information i.e., wave height, flow velocity and arrival times in mins in the SCS. In doing so, it will save at least 2–3 h for evacuation process, and for policymakers to accurately take acting on mitigation strategies along the southern coast of China and eastern coast of Vietnam.

Our efficiency tests suggest that the slip distribution in the northern segment of Manila trench could be well determined by both the cable-based OBP and GNSS-IR networks within 30 min after the earthquake, as long as some key sites could be strategically deployed. In this framework, we search for a key site that could reconstruct the first-order slip distribution, and work sufficiently well for warning and evacuation purposes, and therefore save the overall cost of the limited governmental budget. For the cable-based OBP network, we test each OBP gauge named from C19 to C23 (Figs. 1 and 10a). We find that C21 can almost reconcile the hypothetical slip distribution, and is thus the primary location to deploy an OBP gauge for future tsunami warning (Fig. 10 a and c, S9). For the GNSS-IR network, the optimal station is R12 which locates at a volcanic island in the Luzon strait (Fig. 10 c and d). Although R12 performs slightly less well in reconciling the slip maxima as compared to C21, the derived slip model is sufficient for tsunami forecasting and warning in the SCS (Fig. 10 and S9). All our experimental tests suggest the island-based coastal GNSS-IR network functions comparably well with the cable-based OBP network, even for one single station case.

5.2. Implications of GNSS-IR network for tsunami detecting and warning in the global oceans

The vast portions of the world's subduction zone do not have seismo-geodetic seafloor observational systems like Japan (e.g., GEONET and DONET). These, can effectively and efficiently depict the spatial variable coupling, and estimate slip deficit on the megathrust either for warning or for detailed seismo-tsunamigenic mechanism studies (e.g. Loveless and Meade, 2011, 2010). Alternatively, a successful application of the proposed GNSS-IR network in the SCS could be copied, and implemented elsewhere in the world (Fig. 11). For example, such a network would work particularly well for subduction zones with forearc islands, e.g., the Sumatran subduction zone, where the GNSS network can be deployed on the forearc islands for early detection of approaching tsunami waves from the shallow trench (Fig. 11). This is extremely important for coastlines immediately facing subduction, where forearc islands seating above the seismogenic zone, are prone to megathrust earthquakes at shallow depths but are lack of seafloor monitoring instruments. According to the new map of global islands published by the Association of American Geographers, there are 21,818 big islands (>1 km^2), and 318,868 small islands (<1 km^2) globally with many of them located in the deep-sea region, far away from populous mainland

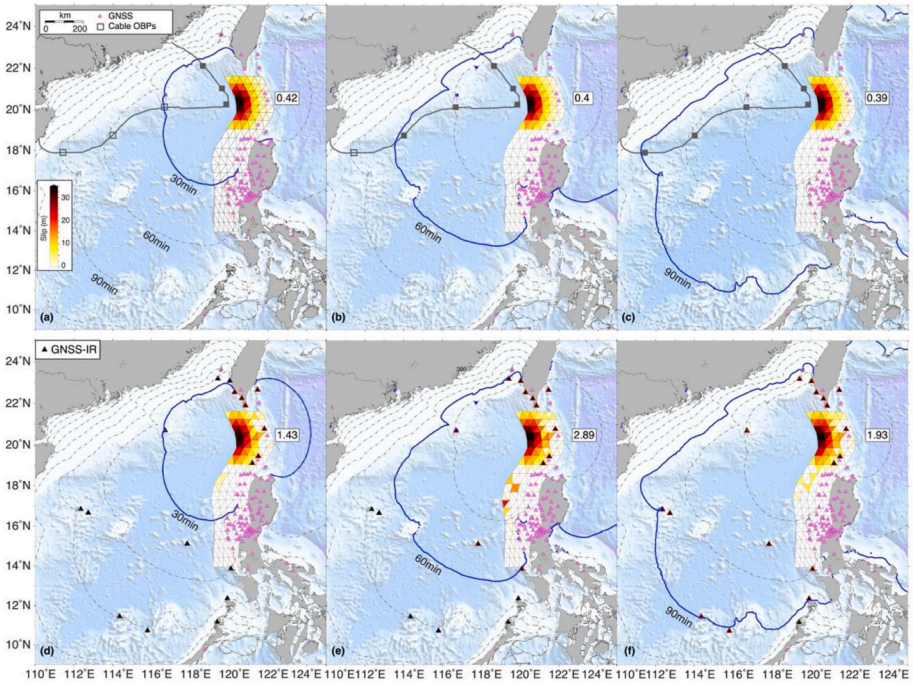

Fig. 9. Efficiency tests for reconstructing the hypothetical slip model for early warning as a demonstration case in the northern segment of the Manila subduction zone when implementing different networks. (a) to (c) the reconstructed slip model using the seafloor cable OBP network and the onshore GNSS sites for the first 30, 60 and 90 min, respectively; (d) to (e) the reconstructed slip model using the onshore GNSS sites and the newly designed GNSS-IR network for the first 30, 60 and 90 min after the hypothetical earthquake, respectively.

(Martin et al., 2020). In the presence of islands close to the active subducting boundary (Fig. 11), like the SCS, Sumatra or western Pacific, an island-based coastal GNSS-IR network could detect tsunami waves tens of mins earlier than DART buoys located seaward of the trench. The network is particularly useful for large-amplitude tsunami waves excited by either a tsunami earthquake or a trench-breaking giant earthquake in the outer wedge of the accretionary prism in the global subduction zones (Hananto et al., 2020; Hubbard et al., 2015; Qiu and Barbot, 2022; Wei et al., 2012). Such early detection efficiency could be also important for regional or transoceanic tsunamis. For instance, a coastal GNSS-IR network in uninhabited islands in the middle of the Pacific Ocean (Fig. 11) should improve tsunami forecasting and warning for the Pacific Tsunami Early Warning system.

An island-based coastal GNSS-IR network could be a promising complement to the existing but still very spatially limited global deep-ocean tsunami monitoring system (Fig. 11). This is mainly due to its following strengthens. First, the cost of a GNSS-IR receiver is significantly cheaper than any of the existing deep-sea tsunami monitoring instruments, e.g., a seafloor-cabled OBP gauge, DART (~US$0.5 M) or a unit of GNSS buoy (~US$3 M) (Bernard and Titov, 2015; González et al., 2005; Mulia and Satake, 2020). Second, the GNSS antenna can be deployed on high ground, and anchored to bedrock rather than on a dock, and is thus far away from vandalism and harsh waves. There are many examples showing that tide gauges could not function properly or failed to record peak wave amplitude during extreme sea-level events e.g., storm surges (Fritz et al., 2010; L. Li et al., 2018b; Soria et al., 2016), and tsunamis (Fritz et al., 2008; Tsushima et al., 2011). A GNSS system is also technically much easier to setup and to maintain than the cabled OBP gauge, and DART stations in the deep ocean. Third, GNSS-IR can operate for decades, offering long-term monitoring of both island's deformation and sea-level changes. Such long-term monitoring power capacities could work together with any seafloor geodetic monitoring system, and onshore GNSS sites to understand the regional tectonics, earthquake mechanisms in seismically active regions. Additionally, the proposed combination of the GNSS-IR and Kalman filtering on monitoring the long-term sea-level changes would contribute to understanding of the regional or global sea-level changes (Han et al., 2021; Hay et al., 2015; Horton et al., 2018). If possible, by combing with the high-frequency Radar measurements, we can measure both the wave height and velocity during extreme sea-level events (Wang et al., 2023). Consequently, coastal GNSS-IR stations could compose a cost-effective and safer network with multiple-disciplinary applications, including tectonics, earthquakes, sea-level variations studies worldwide (https://www.sonel.org/-GPS-.html#map) (Larson et al., 2013; Peng et al., 2019, 2021b).

6. Conclusions

Applying the GNSS-IR technique for measuring either long-term sea-level variations or short-term sea-level extreme events demonstrate that a well-located coastal GNSS site can not only function as a robust tide gauge, but also can suppress the damage from vandalism and harsh sea conditions. In this study, we have shown here that time sampling of the GNSS-IR measurements can be significantly densified with instrumental upgrades so that signals from multiple satellite constellations and frequencies can be used. In the case of SC02, the sampling rates increased dramatically from ~37 min to ~6 min. We also demonstrate that the Kalman filter approach can further regularize densified-irregular sea-level retrievals to an even-sampling rate with small mean, and standard deviation as compared with co-located tide gauge. We investigate the potential application of GNSS-IR technique to tsuami detecting and warning. We show that the combination of the GNSSS-IR determined sea-level retrievals and a Kalman filter can reconstruct a sea-level time series that is equally sampled similar to a conventional tide gauge measurements. This time series can be used to constrain the tsunami source. Our experimental tests from synthetic rupture senarios along the MSZ suggest that such time series are, indeed, powerful to reconcile the tsunami source in the MSZ, which are useful for tsunami forecasting and warning. We propose that the 17 GNSS-IR stations on the island in the SCS can potentially serve as an excellent replacement of deep-sea

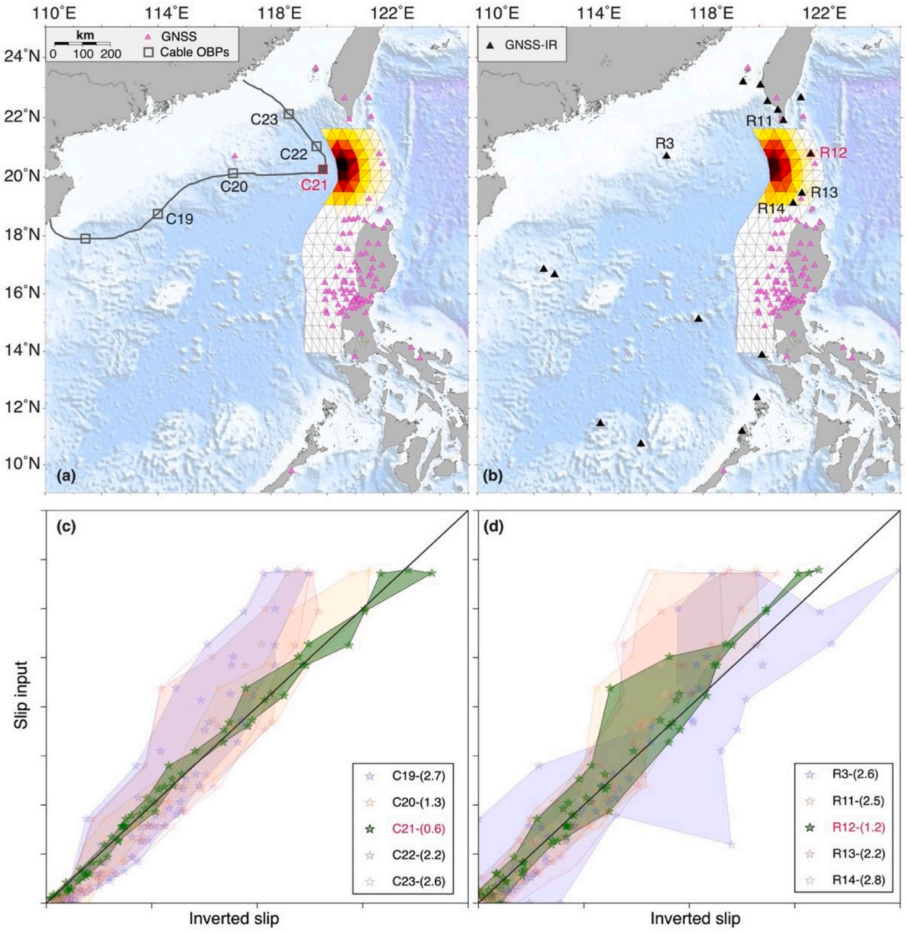

Fig. 10. Key station optimization example for detecting and warning of tsunamis initiated in the northern segment of the Manila subduction zone. (a) the optimized key site (C21) of the seafloor cable OBP network with the efficiency evaluation of each site showing in (c) (i.e., C19 to C23). (b) the optimized site (R12) of the GNSS-IR network with the efficiency evaluation of the near-fault sites i.e., R3, R11, R12 to R14 showing in (d). Each number in the bracket in the legends of (c) to (d) shows the efficiency. The smaller this number, the higher the efficiency in reconstructing the slips on the megathrust. If the station recovers the slip on the fault perfectly, then the stars will align on the black line, otherwise they scatter around the black line. In (c) to (d), the optimized site is highlighted, and the others are shown with transparency.

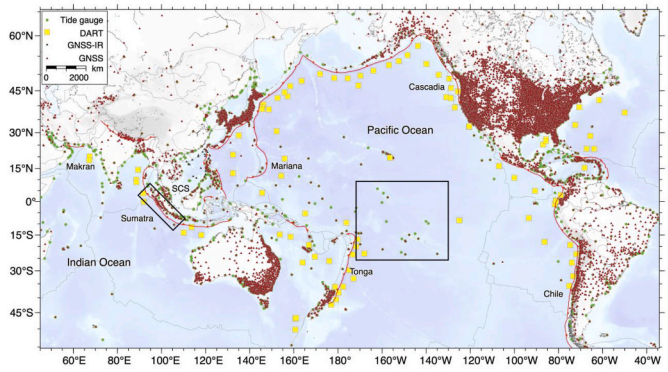

Fig. 11. Global distribution of the DARTs (yellow), tide gauge (light green), GNSS (dark red) and GNSS-IR (light black) for tsunami detecting and warning. Two black boxes show the example of potential GNSS-IR places for tsunami early detecting and warning.

instruments if installing DARTs is impossible. Such a network, if developed on strategically selected islands, can also inexpensively augment the spatial coverage of current DART, and tide gauge system for extreme sea-level event studies worldwide. It also benefits multiple-disciplinary research including the short-term sea-levels detection (i.e., storms and tsunamis) or long-term regional and global sea-level monitoring, and regional tectonic studies.

Open research

All data used in this study are open data sets which can be obtained from https://www.geodetic.gov.hk/sc/rinex/downv.aspx for the HQKT GNSS site, https://www.unavco.org/data/gps-gnss/gps-gnss.html for the SC02 GNSS site, http://www.ioc-sealevelmonitoring.org/map.php for Quarry Bay tide gauge, and http://tidesandcurrents.noaa.gov/waterlevels.html?id59449880) for the Friday Harbor tide gauge. The gnssrefl software is downloaded from https://doi.org/10.5281/zenodo.5601495.

CRediT authorship contribution statement

Linlin Li: Writing – review & editing, Writing – original draft, Methodology, Investigation, Conceptualization. **Qiang Qiu:** Writing – review & editing, Writing – original draft, Methodology, Investigation, Conceptualization. **Mai Ye:** Methodology, Investigation, Formal

analysis, Data curation. **Dongju Peng:** Writing – review & editing, Methodology, Investigation. **Ya-Ju Hsu:** Writing – review & editing, Investigation, Data curation. **Peitao Wang:** Writing – review & editing, Methodology, Data curation. **Huabin Shi:** Writing – review & editing, Methodology, Investigation. **Kristine M. Larson:** Writing – review & editing, Methodology, Formal analysis. **Peizhen Zhang:** Writing – review & editing, Supervision, Conceptualization.

Declaration of competing interest

The authors declare that they have no known competing financial interests or personal relationships that could have appeared to influence the work reported in this paper.

Data availability

Data will be made available on request.

Acknowledgements

We thank Dr. Yuqiang Liu for providing valuable information about the current DART system in the South China Sea. We thank the two anonymous reviewers for their constructive comments which greatly improved our paper. We thank all the researchers, engineers and practitioners who devote great effort to tsunami hazard prevention and mitigation worldwide. This work is funded by Guangdong Province Introduced Innovative R&D Team of Big Data - Mathematical Earth Sciences and Extreme Geological Events Team (2021ZT09H399), National Natural Science Foundation of China (No. 42076059), Innovation Group Project of Southern Marine Science and Engineering Guangdong Laboratory (Zhuhai) (No. 311023002, SML2021SP305), the National Key R&D Program of China (2022YFC3102200, 2022YFC3003804), Chinese Academy of Sciences (Y4SL021, 131551KYSB20200021), the Guangdong Provincial Research and Development Program in key areas (2020B1111520001).

Appendix A. Supplementary data

Supplementary data to this article can be found online at https://doi.org/10.1016/j.coastaleng.2024.104501.

References

An, C., Liu, P.L.-F., Meng, L., 2018. A sensitivity analysis of tsunami inversions on the number of stations. Geophys. J. Int. 214, 1313–1323. https://doi.org/10.1093/gji/ggy212.

Aoi, S., Asano, Y., Kunugi, T., Kimura, T., Uehira, K., Takahashi, N., Ueda, H., Shiomi, K., Matsumoto, T., Fujiwara, H., 2020. MOWLAS: NIED observation network for earthquake, tsunami and volcano. Earth Planets Space 721 (72), 1–31. https://doi.org/10.1186/S40623-020-01250-X, 2020.

Bennett, G.G., 1982. The calculation of astronomical refraction in marine navigation. J. Navig. 35, 255–259.

Bernard, E., Titov, V., 2015. Evolution of tsunami warning systems and products. Philos. Trans. R. Soc. A Math. Phys. Eng. Sci. 373 https://doi.org/10.1098/RSTA.2014.0371.

Böhm, J., Möller, G., Schindelegger, M., Pain, G., Weber, R., 2015. Development of an improved empirical model for slant delays in the troposphere (GPT2w). GPS Solut. 19, 433–441. https://doi.org/10.1007/s10291-014-0403-7.

Chen, K., Liu, Z., Song, Y.T., 2020. Automated GNSS and teleseismic earthquake inversion (AutoQuake inversion) for tsunami early warning: retrospective and real-time results. Pure Appl. Geophys. 177, 1403–1423. https://doi.org/10.1007/S00024-019-02252-X/FIGURES/11.

Data Buoy Cooperation Panel, 2011. Ocean Data Buoy Vandalism-Incidence, Impact and Responses.

Fritz, H.M., Blount, C.D., Albusaidi, F.B., Al-Harthy, A.H.M., 2010. Cyclone Gonu storm surge in Oman. Estuar. Coast Shelf Sci. 86, 102–106. https://doi.org/10.1016/J.ECSS.2009.10.019.

Fritz, Hermann M., Kalligeris, Nikos, Borrero, Jose C., Broncano, Pablo, Ortega, Erick, Fritz, H.M., Kalligeris, N., Borrero, J.C., Broncano, P., Ortega, E., 2008. The 15 August 2007 Peru tsunami runup observations and modeling. Geophys. Res. Lett. 35, 10604 https://doi.org/10.1029/2008GL033494.

Gee, M.J.R., Uy, H.S., Warren, J., Morley, C.K., Lambiase, J.J., 2007. The Brunei slide: a giant submarine landslide on the North West Borneo Margin revealed by 3D seismic data. Mar. Geol. 246, 9–23. https://doi.org/10.1016/j.margeo.2007.07.009.

González, F.I., Bernard, E.N., Meinig, C., Eble, M.C., Mofjeld, H.O., Stalin, S., 2005. The NTHMP tsunameter network. Nat. Hazards 351 (35), 25–39. https://doi.org/10.1007/S11069-004-2402-4, 2005.

Han, S.C., Ghobadi-Far, K., Yeo, I.Y., McCullough, C.M., Lee, E., Sauber, J., 2021. GRACE Follow-On revealed Bangladesh was flooded early in the 2020 monsoon season due to premature soil saturation. Proc. Natl. Acad. Sci. U. S. A. 118, e2109086118 https://doi.org/10.1073/PNAS.2109086118/SUPPL_FILE/PNAS.2109086118.SAPP.PDF.

Hananto, N.D., Leclerc, F., Li, L., Etchebes, M., Carton, H., Tapponnier, P., Qin, Y., Avianto, P., Singh, S.C., Wei, S., 2020. Tsunami earthquakes: vertical pop-up expulsion at the forefront of subduction megathrust. Earth Planet Sci. Lett. 538, 116197 https://doi.org/10.1016/J.EPSL.2020.116197.

Hay, C.C., Morrow, E., Kopp, R.E., Mitrovica, J.X., 2015. Probabilistic reanalysis of twentieth-century sea-level rise. Nature 517, 481–484.

Hill, E.M., Borrero, J.C., Huang, Z., Qiu, Q., Banerjee, P., Natawidjaja, D.H., Elosegui, P., Fritz, H.M., Suwargadi, B.W., Pranantyo, I.R., Li, L., Macpherson, K.A., Skanavis, V., Synolakis, C.E., Sieh, K., 2012. The 2010 M w 7.8 Mentawai earthquake: very shallow source of a rare tsunami earthquake determined from tsunami field survey and near-field GPS data. J. Geophys. Res. B Solid Earth 117. https://doi.org/10.1029/2012JB009159.

Hong Nguyen, P., Cong Bui, Q., Ha Vu, P., The Pham, T., 2014. Scenario-based tsunami hazard assessment for the coast of Vietnam from the Manila Trench source. Phys. Earth Planet. In. 236, 95–108. https://doi.org/10.1016/j.pepi.2014.07.003.

Horton, B.P., Kopp, R.E., Garner, A.J., Hay, C.C., Khan, N.S., Roy, K., Shaw, T.A., 2018. Mapping Sea-level change in time, Space, and probability. Annu. Rev. Environ. Resour. 43, 481–521. https://doi.org/10.1146/annurev-environ-102017-025826.

Hsu, Y.-J., Yu, S.-B., Loveless, J.P., Bacolcol, T., Solidum, R., Luis Jr., A., Pelicano, A., Woessner, J., 2016. Interseismic deformation and moment deficit along the Manila subduction zone and the Philippine Fault system. J. Geophys. Res. Solid Earth 121, 7639–7665. https://doi.org/10.1002/2016JB013082.

Hsu, Y.-J., Yu, S.-B., Song, T.-R.A., Bacolcol, T., 2012. Plate coupling along the Manila subduction zone between Taiwan and northern Luzon. J. Asian Earth Sci. 51, 98–108. https://doi.org/10.1016/j.jseaes.2012.01.005.

Hubbard, J., Barbot, S., Hill, E.M., Tapponnier, P., 2015. Coseismic slip on shallow décollement megathrusts: implications for seismic and tsunami hazard. Earth Sci. Rev. 141, 45–55. https://doi.org/10.1016/J.EARSCIREV.2014.11.003.

Kalman, R.E., 1960. A new approach to linear filtering and prediction problems. J. Basic Eng. 82, 35–45. https://doi.org/10.1115/1.3662552.

Kanazawa, T., 2013. Japan Trench earthquake and tsunami monitoring network of cable-linked 150 ocean bottom observatories and its impact to earth disaster science. In: 2013 IEEE Int. Underw. Technol. Symp. UT 2013. https://doi.org/10.1109/UT.2013.6519911.

Karegar, M.A., Kusche, J., Geremia-Nievinski, F., Larson, K.M., 2022. Raspberry pi reflector (RPR): a low-cost water-level monitoring system based on GNSS interferometric reflectometry. Water Resour. Res. 58, e2021WR031713 https://doi.org/10.1029/2021WR031713.

Larson, K.M., Lay, T., Yamazaki, Y., Cheung, K.F., Ye, L., Williams, S.D.P., Davis, J.L., 2021a. Dynamic Sea level variation from GNSS: 2020 shumagin earthquake tsunami resonance and Hurricane Laura. Geophys. Res. Lett. 48, e2020GL091378 https://doi.org/10.1029/2020GL091378.

Larson, K.M., Lay, T., Yamazaki, Y., Cheung, K.F., Ye, L., Williams, S.D.P., Davis, J.L., 2021b. Dynamic Sea level variation from GNSS: 2020 shumagin earthquake tsunami resonance and Hurricane Laura. Geophys. Res. Lett. 48, e2020GL091378 https://doi.org/10.1029/2020GL091378.

Larson, K.M., Ray, R.D., Nievinski, F.G., Freymueller, J.T., 2013. The accidental tide gauge: a GPS reflections case study from kachemak Bay, Alaska. Geosci. Rem. Sens. Lett. IEEE 10, 1200–1204. https://doi.org/10.1109/lgrs.2012.2236075.

Larson, K.M., Ray, R.D., Williams, S.D.P., 2017. A 10-year comparison of water levels measured with a geodetic GPS receiver versus a conventional tide gauge. J. Atmos. Ocean. Technol. 34, 295–307. https://doi.org/10.1175/JTECH-D-16-0101.1.

Lay, T., 2018. A review of the rupture characteristics of the 2011 Tohoku-oki Mw 9.1 earthquake. Tectonophysics 733, 4–36. https://doi.org/10.1016/J.TECTO.2017.09.022.

Li, J., Ding, W., Lin, J., Xu, Y., Kong, F., Li, S., Huang, X., Zhou, Z., 2021. Dynamic processes of the curved subduction system in Southeast Asia: a review and future perspective. Earth Sci. Rev. 217, 103647 https://doi.org/10.1016/J.EARSCIREV.2021.103647.

Li, L., Qiu, Q., Li, Z., Zhang, P., 2022. Tsunami hazard assessment in the South China Sea: a review of recent progress and research gaps. Sci. China Earth Sci. 655 (65), 783–809. https://doi.org/10.1007/S11430-021-9893-8, 2022.

Li, L., Shi, F., Ma, G., Qiu, Q., 2019. Tsunamigenic potential of the baiyun slide complex in the South China sea. J. Geophys. Res. Solid Earth 124, 7680–7698. https://doi.org/10.1029/2019jb018062.

Li, L., Switzer, A.D., Chan, C.-H., Wang, Y., Weiss, R., Qiu, Q., 2016. How heterogeneous coseismic slip affects regional probabilistic tsunami hazard assessment: a case study in the South China Sea. J. Geophys. Res. Solid Earth 2016JB013111-T. https://doi.org/10.1002/2016JB013111.

Li, L., Switzer, A.D., Wang, Y., Chan, C.-H., Qiu, Q., Weiss, R., 2018a. A modest 0.5-m rise in sea level will double the tsunami hazard in Macau. Sci. Adv. 4 https://doi.org/10.1126/sciadv.aat1180.

Li, L., Yang, J., Lin, C.Y., Ting Chua, C., Wang, Y., Zhao, K., Wu, Y.T., Li-Fan Liu, P., Switzer, A.D., Meng Mok, K., Wang, P., Peng, D., 2018b. Field survey of Typhoon

Hato (2017) and a comparison with storm surge modeling in Macau. Nat. Hazards Earth Syst. Sci. 18, 3167–3178. https://doi.org/10.5194/NHESS-18-3167-2018.
Li, Z.-S., Zhao, X., An, C., Liu, H., 2018. Wave profiles of a virtual extreme tsunami in the northern region of south China sea. J. Earthq. Tsunami 12, 1840004. https://doi.org/10.1142/S1793431118400043.
Liu, P.L.-F., Cho, Y.-S., Briggs, M.J., Kanoglu, U., Synolakis, C.E., 1995. Runup of solitary waves on a circular island. J. Fluid Mech. 302, 259–285.
Liu, P.L.F., Wang, X., Salisbury, A.J., 2009. Tsunami hazard and early warning system in South China Sea. J. Asian Earth Sci. 36, 2–12. https://doi.org/10.1016/j.jseaes.2008.12.010.
Loveless, J.P., Meade, B.J., 2011. Spatial correlation of interseismic coupling and coseismic rupture extent of the 2011 MW = 9.0 Tohoku-oki earthquake. Geophys. Res. Lett. 38, L17306 https://doi.org/10.1029/2011GL048561.
Loveless, J.P., Meade, B.J., 2010. Geodetic Imaging of Plate Motions, Slip Rates, and Partitioning of Deformation in Japan, vol. 115, B02410. https://doi.org/10.1029/2008JB006248.
Martin, M., Sayre, R., VanGraafeiland, K., McDermott Long, O., Weatherdon, L., Will, D., Spatz, D.R., Holmes, N.D., 2020. Global islands. Encycl. World's Biomes 47–50. https://doi.org/10.1016/B978-0-12-409548-9.12475-3.
Megawati, K., Shaw, F., Sieh, K., Huang, Z., Wu, T.-R., Lin, Y., Tan, S.K., Pan, T.-C., 2009. Tsunami hazard from the subduction megathrust of the South China Sea: Part I. Source characterization and the resulting tsunami. J. Asian Earth Sci. 36, 13–20.
Mori, N., Satake, K., Cox, D., Goda, K., Catalan, P.A., Ho, T.-C., Imamura, F., Tomiczek, T., Lynett, P., Miyashita, T., Muhari, A., Titov, V., Wilson, R., 2022. Giant tsunami monitoring, early warning and hazard assessment. Nat. Rev. Earth Environ. 2022, 1–16. https://doi.org/10.1038/s43017-022-00327-3.
Mulia, I.E., Satake, K., 2020. Developments of tsunami observing systems in Japan. Front. Earth Sci. 8, 145. https://doi.org/10.3389/FEART.2020.00145/XML/NLM.
Peng, D., Feng, L., Larson, K.M., Hill, E.M., 2021a. Measuring coastal absolute sea-level changes using GNSS interferometric reflectometry. Rem. Sens. 13, 4319. https://doi.org/10.3390/rs13214319.
Peng, D., Feng, L., Larson, K.M., Hill, E.M., Vigo, I., Fernandes, J., García-García, D., Darrozes, J., Blarel, F., Normandin, C., Shu, S., Huang, W., 2021b. Measuring coastal absolute sea-level changes using GNSS interferometric reflectometry. Rem. Sens. 13, 4319. https://doi.org/10.3390/RS13214319, 4319 13.
Peng, D., Hill, E.M., Li, L., Switzer, A.D., Larson, K.M., 2019. Application of GNSS interferometric reflectometry for detecting storm surges. GPS Solut. 23, 47. https://doi.org/10.1007/s10291-019-0838-y.
Peng, D., Soon, K.Y., Khoo, V.H.S., Mulder, E., Wong, P.W., Hill, E.M., 2023. Tidal asymmetry and transition in the Singapore Strait revealed by GNSS interferometric reflectometry. Geosci. Lett.
Philibosian, B., Meltzner, A.J., 2020. Segmentation and supercycles: a catalog of earthquake rupture patterns from the Sumatran Sunda Megathrust and other well-studied faults worldwide. Quat. Sci. Rev. 241, 106390 https://doi.org/10.1016/J.QUASCIREV.2020.106390.
Power, W., Wallace, L., Wang, X., Reyners, M., 2012. Tsunami hazard posed to New Zealand by the kermadec and southern new hebrides subduction margins: an assessment based on plate boundary kinematics, interseismic coupling, and historical seismicity. Pure Appl. Geophys. 169, 1–36. https://doi.org/10.1007/s00024-011-0299-x.
Qiu, Q., Barbot, S., 2022. Tsunami excitation in the outer wedge of global subduction zones. Earth Sci. Rev. 230, 104054 https://doi.org/10.1016/j.earscirev.2022.104054.
Qiu, Q., Feng, L., Hermawan, I., Hill, E.M., 2019a. Coseismic and postseismic slip of the 2005 M w 8.6 nias-simeulue earthquake: spatial overlap and localized viscoelastic flow. J. Geophys. Res. Solid Earth 124, 7445–7460. https://doi.org/10.1029/2018JB017263.
Qiu, Q., Li, L., Hsu, Y.-J., Wang, Y., Chan, C.-H., Switzer, A.D., 2019b. Revised earthquake sources along Manila trench for tsunami hazard assessment in the South China Sea. Nat. Hazards Earth Syst. Sci. 19, 1565–1583.
Rauch, H.E., Tung, F., Striebel, C.T., 1965. Maximum likelihood estimates of linear dynamic systems. AIAA J. 3, 1445–1450. https://doi.org/10.2514/3.3166.
Roesler, C., Larson, K.M., 2018. Software tools for GNSS interferometric reflectometry (GNSS-IR). GPS Solut. 22, 1–10. https://doi.org/10.1007/S10291-018-0744-8/FIGURES/9.
Satake, K., Fujii, Y., Harada, T., Namegaya, Y., 2013. Time and Space distribution of coseismic slip of the 2011 Tohoku earthquake as inferred from tsunami waveform data. Bull. Seismol. Soc. Am. 103, 1473–1492. https://doi.org/10.1785/0120120122.
Satake, K., Tanioka, Y., 1999. Sources of tsunami and tsunamigenic earthquakes in subduction zones. Pure Appl. Geophys. 154, 467–483. https://doi.org/10.1007/s000240050240.
Sepúlveda, I., Cao, B., Haase, J.S., Murphy, M.J., 2023. Optimizing simultaneous water level and wave measurements from multi-GNSS interferometric reflectometry over 1 Year at an exposed coastal site. Earth Space Sci. 10, e2022EA002767 https://doi.org/10.1029/2022EA002767.
Sepúlveda, I., Liu, P.L.-F., Grigoriu, M., 2019. Probabilistic tsunami hazard assessment in south China sea with consideration of uncertain earthquake characteristics. J. Geophys. Res. Solid Earth 124, 658–688. https://doi.org/10.1029/2018JB016620.
Soria, J.L.A., Switzer, A.D., Villanoy, C.L., Fritz, H.M., Bilgera, P.H.T., Cabrera, O.C., Siringan, F.P., Maria, Y.Y.S., Ramos, R.D., Fernandez, I.Q., 2016. Repeat storm surge disasters of typhoon haiyan and its 1897 predecessor in the Philippines. Bull. Am. Meteorol. Soc. 97, 31–48. https://doi.org/10.1175/BAMS-D-14-00245.1.
Strandberg, J., Hobiger, T., Haas, R., 2019. Real-time sea-level monitoring using Kalman filtering of GNSS-R data. GPS Solut. 23, 61. https://doi.org/10.1007/s10291-019-0851-1.
Sun, Q., Cartwright, J., Xie, X., Lu, X., Yuan, S., Chen, C., 2018. Reconstruction of repeated Quaternary slope failures in the northern South China Sea. Mar. Geol. 401, 17–35. https://doi.org/10.1016/j.margeo.2018.04.009.
Tabibi, S., Geremia-Nievinski, F., Francis, O., van Dam, T., 2020. Tidal analysis of GNSS reflectometry applied for coastal sea level sensing in Antarctica and Greenland. Remote Sens. Environ. 248, 111959 https://doi.org/10.1016/J.RSE.2020.111959.
Tang, L., Titov, V.V., Bernard, E.N., Wei, Y., Chamberlin, C.D., Newman, J.C., Mofjeld, H. O., Arcas, D., Eble, M.C., Moore, C., Uslu, B., Pells, C., Spillane, M., Wright, L., Gica, E., 2012. Direct energy estimation of the 2011 Japan tsunami using deep-ocean pressure measurements. J. Geophys. Res. Ocean. 117 (8008) https://doi.org/10.1029/2011JC007635.
Terry, J.P., Winspear, N., Goff, J., Tan, P.H.H., 2017. Past and potential tsunami sources in the South China Sea: a brief synthesis. Earth Sci. Rev. 167, 47–61. https://doi.org/10.1016/j.earscirev.2017.02.007.
Tsushima, H., Hirata, K., Hayashi, Y., Tanioka, Y., Kimura, K., Sakai, S., Shinohara, M., Kanazawa, T., Hino, R., Maeda, K., 2011. Near-field tsunami forecasting using offshore tsunami data from the 2011 off the Pacific coast of Tohoku Earthquake. Earth Planets Space 63, 821–826. https://doi.org/10.5047/EPS.2011.06.052/FIGURES/3.
Vu, P.L., Ha, M.C., Frappart, F., Darrozes, J., Ramillien, G., Dufrechou, G., Gegout, P., Morichon, D., Bonneton, P., 2019. Identifying 2010 xynthia storm signature in GNSS-R-based tide records. Rem. Sens. 11, 782. https://doi.org/10.3390/RS11070782, 782 11.
Wang, W., Wang, D., Wu, S., Völker, D., Zeng, H., Cai, G., Li, Q., 2018. Submarine Landslides on the North Continental Slope of the South China Sea. https://doi.org/10.1007/s11802-018-3491-0.
Wang, X., He, X., Shi, J., Chen, S., Niu, Z., 2022. Estimating sea level, wind direction, significant wave height, and wave peak period using a geodetic GNSS receiver. Remote Sens. Environ. 279, 113135 https://doi.org/10.1016/J.RSE.2022.113135.
Wang, X., Liu, P.L.-F., 2007. Numerical simulations of the 2004 Indian ocean tsunamis — coastal effects. J. Earthq. Tsunami 1, 273–297. https://doi.org/10.1142/S179343110700016X.
Wang, X., Liu, P.L.F., 2006. An analysis of 2004 Sumatra earthquake fault plane mechanisms and Indian Ocean tsunami. J. Hydraul. Res. 44, 147–154.
Wang, Y., Imai, K., Mulia, I.E., Ariyoshi, K., Takahashi, N., Sasaki, K., Kaneko, H., Abe, H., Sato, Y., 2023. Data assimilation using high-frequency radar for tsunami early warning: a case study of the 2022 Tonga volcanic tsunami. J. Geophys. Res. Solid Earth 128, e2022JB025153. https://doi.org/10.1029/2022JB025153.
Wang, Y., Tsushima, H., Satake, K., Navarrete, P., 2021. Review on recent progress in near-field tsunami forecasting using offshore tsunami measurements: source inversion and data assimilation. Pure Appl. Geophys. 178, 5109–5128. https://doi.org/10.1007/S00024-021-02910-Z, 2021 17812.
Wang, Y., Zamora, N., Quiroz, M., Satake, K., Cienfuegos, R., 2021. Tsunami resonance characterization in Japan due to trans-pacific sources: response on the Bay and continental shelf. J. Geophys. Res. Ocean. 126, e2020JC017037 https://doi.org/10.1029/2020JC017037.
Wei, S., Graves, R., Helmberger, D., Avouac, J.-P., Jiang, J., 2012. Sources of shaking and flooding during the Tohoku-Oki earthquake: a mixture of rupture styles. Earth Planet Sci. Lett. 333–334, 91–100. https://doi.org/10.1016/j.epsl.2012.04.006.
Wei, Y., Bernard, E.N., Tang, L., Weiss, R., Titov, V.V., Moore, C., Spillane, M., Hopkins, M., Kânoğlu, U., 2008. Real-time experimental forecast of the Peruvian tsunami of August 2007 for U.S. coastlines. Geophys. Res. Lett. 35, 4609. https://doi.org/10.1029/2007GL032250.
Williams, S.D.P., Nievinski, F.G., 2017. Tropospheric delays in ground-based GNSS multipath reflectometry—experimental evidence from coastal sites. J. Geophys. Res. Solid Earth 122, 2310–2327. https://doi.org/10.1002/2016JB013612.
Williamson, A.L., Melgar, D., Crowell, B.W., Arcas, D., Melbourne, T.I., Wei, Y., Kwong, K., 2020. Toward near-field tsunami forecasting along the cascadia subduction zone using rapid GNSS source models. J. Geophys. Res. Solid Earth 125, e2020JB019636. https://doi.org/10.1029/2020JB019636.
Xia, S., Zhou, P., Zhao, D., Cao, J., 2020. Seismogenic structure in the source zone of the 1918 M7.5 NanAo earthquake in the northern South China Sea. Phys. Earth Planet. In. 302, 106472 https://doi.org/10.1016/j.pepi.2020.106472.
Xu, Z., Liang, S., Abd Rahman, M.N. Bin, Li, H., Shi, J., 2021. Historical earthquakes, tsunamis and real-time earthquake monitoring for tsunami advisory in the South China Sea region. Nat. Hazards 107, 771–793. https://doi.org/10.1007/S11069-021-04605-Z/FIGURES/10.
Yang, X., Qiu, Q., Feng, W., Lin, J., Zhang, J., Zhou, Z., Zhang, F., 2022. Mechanism of the 2017 Mw 6.3 Pasni earthquake and its significance for future major earthquakes in the eastern Makran. Geophys. J. Int. https://doi.org/10.1093/gji/ggac257.
Yuan, Y., Li, H., Wei, Y., Shi, F., Wang, Z., Hou, J., Wang, P., Xu, Z., 2021. Probabilistic tsunami hazard assessment (PTHA) for southeast coast of Chinese mainland and taiwan island. J. Geophys. Res. Solid Earth 126, e2020JB020344. https://doi.org/10.1029/2020JB020344.
Zhang, X., Niu, X., 2020. Probabilistic tsunami hazard assessment and its application to southeast coast of Hainan Island from Manila Trench. Coast. Eng. 155, 103596 https://doi.org/10.1016/J.COASTALENG.2019.103596.